Reconstructing cerebrovascular networks under local physiological constraints by integer programming

Markus Rempfler [a,b,*], Matthias Schneider [b,c], Giovanna D. Ielacqua [d], Xianghui Xiao [e], Stuart R. Stock [f], Jan Klohs [d], Gábor Székely [b], Bjoern Andres [g], Bjoern H. Menze [a,h]

[a] Department of Computer Science, Technische Universität München, Germany
[b] Computer Vision Laboratory, ETH Zürich, Switzerland
[c] Institute of Pharmacology and Toxicology, University of Zürich, Switzerland
[d] Institute for Biomedical Engineering, University and ETH Zürich, Switzerland
[e] Advanced Photon Source, Argonne National Laboratory, Lemont, IL, USA
[f] Feinberg School of Medicine, Northwestern University, Chicago, IL, USA
[g] Max Planck Institute for Informatics, Saarbrücken, Germany
[h] Institute for Advanced Studies, Technische Universität München, Germany

ARTICLE INFO

ABSTRACT

We introduce a probabilistic approach to vessel network extraction that enforces physiological constraints on the vessel structure. The method accounts for both image evidence and geometric relationships between vessels by solving an integer program, which is shown to yield the maximum a posteriori (MAP) estimate to a probabilistic model. Starting from an overconnected network, it is pruning vessel stumps and spurious connections by evaluating the local geometry and the global connectivity of the graph. We utilize a high-resolution micro computed tomography (μCT) dataset of a cerebrovascular corrosion cast to obtain a reference network and learn the prior distributions of our probabilistic model and we perform experiments on in-vivo magnetic resonance microangiography (μMRA) images of mouse brains. We finally discuss properties of the networks obtained under different tracking and pruning approaches.

1. Introduction

Many diseases affect general properties of the cerebrovascular network, examples are arteriosclerosis and dilative vascular malformations changing vessel shape and diameter, but also Alzheimer's and related neuro-degenerative diseases are suspected to affect the general vascularity and global network properties (Hunter et al., 2012; Klohs et al., 2012). Studies investigating such diseases frequently use mouse models for experiments and commonly acquire in-vivo cerebrovascular imagery by means of magnetic resonance microangiography (μMRA). While segmenting and tracing tubular structures is a longstanding field of interest in medical image computing (Aylward and Bullitt, 2002; Frangi et al., 1998; Kirbas and Quek, 2004; Lesage et al., 2009), we approach here the wider – and somewhat neglected (Jiang et al., 2010) – problem of extracting the full vascular network from image volumes under consideration of local geometric properties and global constraints of the vascular structure.

Most vessel segmentation techniques rely on tubularity measures or other vessel enhancement filters (Frangi et al., 1998), and then apply rule-based or learned decision algorithms to segment the vessels (Kirbas and Quek, 2004; Lesage et al., 2009; Schneider et al., 2015). The network graph – representing vessels by their centerline, complemented with additional information such as local radii – can be extracted from binary segmentations using morphological operators (Lee et al., 1994; Pudney, 1998), or by tracking vessels directly by minimal path techniques (Cohen and Kimmel, 1997), e.g. by applying a fast marching algorithm (Benmansour and Cohen, 2011) or a Dijkstra-like scheme (Gülsün and Tek, 2008). We point the interested reader to Kirbas and Quek (2004) and Lesage et al. (2009) for more extensive reviews. In most applications, however, the extracted graphs need further post-processing: Lu et al. (2009), for example, incorporated discriminative classifiers that examine local geometrical features of segments into a hierarchical approach for vessel-structure parsing. In order to deal with imperfections in vascular connectivity of extracted networks, Kaufhold et al. (2012) discussed a supervised learning approach to gap filling and network pruning, whereas Schneider et al. (2014) recently proposed a generative method for gap in-fill that is guided by a simplified angiogenesis model. While segmentation

* Corresponding author at: IMETUM, Boltzmannstr. 11, 85748 Garching, Germany.
Tel.: +49 8928910840.
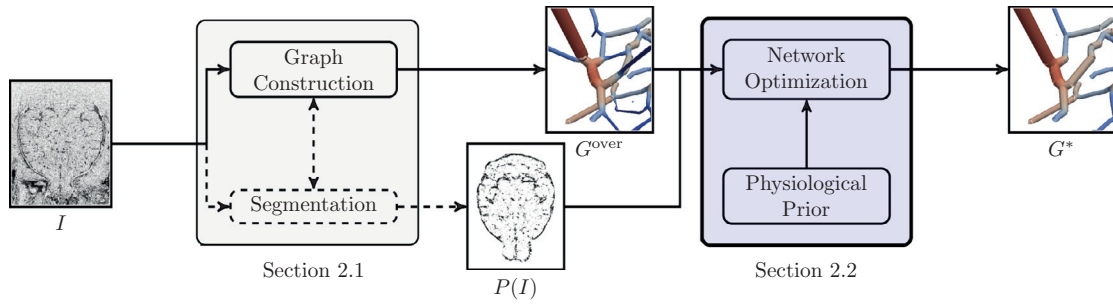*E-mail address:* markurem@vision.ee.ethz.ch (M. Rempfler).

Fig. 1. Workflow: In a first stage, the image volume I is processed so as to obtain an overconnected graph G^{over} as well as a confidence measure for vessels such as the confidence map $P(I)$. In the following step, the network $G*$ is extracted from G^{over} in an optimization scheme that considers both image evidence (according to $P(I)$) and geometric-physiological prior knowledge. In this paper, we focus on the network optimization step, where both image evidence and geometrical relationships of certain network motifs, namely continuing pairs and bifurcations are considered.

algorithms are likely to enforce expected local vessel shape and geometry, only few approaches consider both local properties and global network connectivity when extracting the full network: Jiang et al. (2011) incorporated assumptions about vessel diameters (Murray's hypothesis (Murray, 1926)) in a global optimization problem restricted to vascular trees. Tree shape priors have also been included into the segmentation of vasculature by Stühmer et al. (2013). In a different application, Türetken et al. (2015) introduced recently an integer programming approach that evaluates path coherence and connectivity of general curvilinear structures, such as streets in remote-sensing images or vessels in confocal image stacks. Starting from an overconnected graph, they are pruning edges that do not fulfill desired structural relationships of neighboring segment pairs using a path classifier that is trained from annotated 3-D networks.

All of these approaches enforce local coherence within the extracted network – a general property of the vascular network. More complex local properties of a structural network, however, can be described by network *motifs* (Alon, 2007; Milo et al., 2002). Network motifs are frequently recurring subgraphs, also called building blocks, that are characteristic for a type of network, such as bifurcations in vascular networks.

In this paper, we enforce local geometrical properties similar to Jiang et al. (2011), exploring the relevance of two basic motifs of vascular networks, i.e., the geometrical properties of continuing segment pairs and of vessel bifurcations and following the idea of pruning of Türetken et al. (2015). We present a probabilistic model which combines this geometric prior with local vessel evidence obtained from a segmentation algorithm (Schneider et al., 2015), and show that the maximum a posteriori (MAP) estimate can be computed by an integer linear program (ILP). We learn the global statistic of geometrical properties of the network motifs from a high resolution dataset. Finally, we identify a more efficient scheme to solve the ILP for large datasets and illustrate its application for reconstructing vascular networks from in-vivo μMRA images of the mouse brain.

2. Methods

In this section, we detail on the proposed vessel network extraction method that estimates the most probable network under consideration of image evidence and physiological prior knowledge. As depicted in the workflow (Fig. 1), this method starts from an overconnected network graph G^{over}. Hence, we briefly review the applied segmentation framework and skeletonization method as used in our experiments.

2.1. Vessel segmentation method and construction of the overconnected graph

As a first stage, we transform image intensities into confidence maps by using the framework of Schneider et al. (2013, 2015): In

$$I, G \longrightarrow X \longrightarrow \Omega$$

Fig. 2. Probabilistic model. I: Image; G: (overconnected) Graph; X: Set of binary variables denoting subgraphs of G; Ω: Set of feasible configurations of **x**.

this approach, multiscale steerable filter templates (SFT) are used as efficient directional filters, offering features that are invariant with respect to the local vessel direction. An oblique random forest (RF) (Menze et al., 2011), which determines splits by solving a linear regression with elastic net penalty in each node, is used for a subsequent classification. The RF assigns each voxel v in an image volume I to a probability $p_v \in [0, 1]$, indicating the local presence of a vessel-like structure.

We apply a threshold θ to the probability volume $P(I)$ and skeletonize the resulting binary volume using distance-ordered homotopic thinning (DOHT) (Pudney, 1998), a method that iteratively removes voxels without altering the objects topology, to derive a network graph $G(\theta)$. We obtain an overconnected network by generating multiple binary segmentations from $P(I)$ with different thresholds $\{\theta_i\}$, skeletonizing each of them by DOHT to $G(\theta_i)$ and superposing them into one network $G^{over}(\{\theta_i\})$. The resulting network contains both segments with low confidence (contributed by graphs from low thresholds θ close to 0), but maintains the high spatial accuracy of a graph that is generated from conservative thresholds (i.e., with θ close to 1). Note, however, that any method which generates an overconnected graph G^{over} by proposing local vessel connections could be used instead.

2.2. Vessel network extraction

The goal of our method is to find the most plausible network $G*$ out of an overconnected network graph $G^{over} = (V, E)$ with edges $E = \{e_i\}$ and given image evidence $P(I)$. We encode subgraphs of G^{over} with a set of binary variables $X = \{x_i\}$ where each x_i indicates whether or not the corresponding segment $e_i \in E$ is active (i.e. $x_i = 1$). Therefore, we arrive at the equivalent problem of determining the MAP estimate of $\mathbf{x} \in \{0, 1\}^{|E|}$, for which we describe a probabilistic model (Section 2.2.1) that considers image evidence, local properties of specific network motifs as well as global connectivity, and derive an ILP that allows computing the MAP network (Section 2.2.2).

2.2.1. Probabilistic model

We formulate a probabilistic model $P(\mathbf{X} = \mathbf{x}, \Omega | I, G)$ according to Fig. 2, where I is the image evidence, G is the given (overconnected) graph and X is the set of binary variables denoting subgraphs of G. Ω is the set of all feasible solutions of **x**:

$$\Omega = \{\mathbf{x} \in \{0, 1\}^{|E|} : \mathbf{Ax} \geq \mathbf{b}\}, \tag{1}$$

with $\mathbf{Ax} \geq \mathbf{b}$ being the short notation for all hard constraints that will be considered such as those enforcing connectivity. This introduces a

probabilistic interpretation, as in Qu and Andres (2014), of the hard constraints that we impose on the extracted networks.

According to the given probabilistic model in Fig. 2, we arrive at the posterior distribution for **x**:

$$P\left(\mathbf{X}=\mathbf{x}|I,G,\Omega\right) \propto P\left(\Omega|\mathbf{X}=\mathbf{x}\right)P\left(\mathbf{X}=\mathbf{x}|I,G\right). \quad (2)$$

Next, we model $P(\mathbf{X}=\mathbf{x}|I,G)$ as a Markov random field (MRF):

$$P(\mathbf{X}=\mathbf{x}|I,G) = \frac{1}{Z}\prod_{x_i\in X}\phi_i\left(x_i;I,G\right)^{\alpha}\prod_{\substack{x_i,x_j\in X:\\e_i,e_j\ \text{adjacent}\\\nexists e_k\ \text{adjacent to }e_i\wedge e_j}}$$

$$\phi_{i,j}\left(x_i,x_j;I,G\right)\prod_{\substack{x_i,x_j,x_k\in X:\\e_i,e_j,e_k\ \text{adjacent}}}\phi_{i,j,k}\left(x_i,x_j,x_k;I,G\right), \quad (3)$$

where Z is the partition function and $\phi(.)$ are the potentials, which are defined in the following. $\alpha > 0$ is a parameter to adapt the trade-off between unary and higher order potentials. For each segment represented by x_i, we set the unary potential:

$$\phi_i\left(x_i;I,G\right) = \begin{cases} P\left(x_i=1|I_i,E_i\right) & \text{if } x_i=1, \\ P\left(x_i=0|I_i,E_i\right) & \text{otherwise,} \end{cases} \quad (4)$$

where $P(x_i=1|I_i,E_i)$ can be understood as image evidence that the segment x_i is part of the underlying vasculature and a valid segment of the network. The higher-order potentials are chosen as:

$$\phi_{i,j}\left(x_i,x_j;I,G\right) = \begin{cases} p_{C,ij} & \text{if } x_ix_j=1, \\ p_T & \text{otherwise,} \end{cases} \quad (5)$$

and

$$\phi_{i,j,k}\left(x_i,x_j,x_k;I,G\right) = \begin{cases} p_{B,ijk} & \text{if } x_ix_jx_k=1, \\ p_{C,ij} & \text{if } x_ix_j=1 \wedge x_ix_jx_k=0, \\ p_T & \text{otherwise.} \end{cases} \quad (6)$$

where $p_{C,ij}$ is the likelihood of e_i continuing in e_j, $p_{B,ijk}$ the likelihood of a bifurcation involving e_i, e_j and e_k, and p_T represents the possibility that neither of them occur and the vessel terminates. Note that both binary and ternary potentials in (3) account for the relationships of multiple segments, hence we can split $P(\mathbf{X}=\mathbf{x}|I,G)$ into a pure image evidence term – containing only the unary potentials $\phi_i(.)$ – and a prior term consisting of both $\phi_{i,j}(.)$ and $\phi_{i,j,k}(.)$.

2.2.2. Maximum a posteriori estimation by integer programming

So far, we translated the problem of finding the most plausible subnetwork in G^{over} into determining the MAP estimate $\mathbf{x}^*$ of (2):

$$\mathbf{x}^* = \underset{\mathbf{x}\in\mathcal{X}}{\arg\max}\,P\left(\mathbf{X}=\mathbf{x}|I,G,\Omega\right)$$

$$= \underset{\mathbf{x}\in\mathcal{X}}{\arg\max}\,P\left(\Omega|\mathbf{X}=\mathbf{x}\right)P\left(\mathbf{X}=\mathbf{x}|I,G\right), \quad (7)$$

where $\mathcal{X}=\{0,1\}^{|E|}$ is the set of all configurations of **x**. In the following, we are going to derive an ILP to determine $\mathbf{x}^*$. We start by specifying the likelihood $P(\Omega|\mathbf{X}=\mathbf{x})$ to be equal for all feasible **x** and 0 else, i.e.

$$P(\Omega|\mathbf{X}=\mathbf{x}) \propto \begin{cases} 1 & \text{if } \mathbf{x}\in\Omega, \\ 0 & \text{otherwise.} \end{cases} \quad (8)$$

Applying this definition leads to:

$$\mathbf{x}^* = \underset{\mathbf{x}\in\mathcal{X}}{\arg\max}\,P\left(\Omega|\mathbf{X}=\mathbf{x}\right)P\left(\mathbf{X}=\mathbf{x}|I,G\right) \quad (9)$$

$$= \underset{\mathbf{x}\in\Omega}{\arg\max}\,P(\mathbf{X}=\mathbf{x}|I,G). \quad (10)$$

From (10), the definition of the MRF (3), its potentials (4)–(6) and the fact that each pseudo-boolean function has a unique multilinear polynomial form, it follows that the MAP estimate $\mathbf{x}^*$ takes the form of the integer program:

$$\min_{\mathbf{x}} \; J(\mathbf{x}) = \alpha\sum_{x_i\in X}w_ix_i + \sum_{\substack{x_i,x_j\in X:\\e_i,e_j\ \text{adjacent}}}w_{ij}x_ix_j$$

$$+ \sum_{\substack{x_i,x_j,x_k\in X:\\e_i,e_j,e_k\ \text{adjacent}}}w_{ijk}x_ix_jx_k, \quad (11)$$

$$\text{s.t.}\quad \mathbf{Ax}\geq\mathbf{b}, \quad (12)$$

$$x_i\in\{0,1\}\quad\forall x_i\in X, \quad (13)$$

with the weights w_i, w_{ij} and w_{ijk} derived as

$$w_i = -\log\frac{P\left(x_i=1|I_i,E_i\right)}{P\left(x_i=0|I_i,E_i\right)}, \quad (14)$$

$$w_{ij} = -\log\frac{p_{C,ij}}{p_T}, \quad (15)$$

$$w_{ijk} = -\log\frac{p_{B,ijk}p_T^2}{p_{C,ij}p_{C,ik}p_{C,jk}}. \quad (16)$$

The derivation is given in Appendix A.

2.2.3. Computing the weights

Image Evidence. The weights derived from the unary potentials of the MRF allow us to account for image evidence observed for each segment represented by x_i separately. To infer $P(x_i=1|I_i,E_i)$ from the image evidence, we average the probabilistic output p_v of the classification along voxels v assigned to the segment e_i. We define $P(x_i=1|I_i,E_i)=p_i$ and compute:

$$w_i = -\log\frac{p_i}{1-p_i}. \quad (17)$$

Geometric prior. As depicted in Fig. 3, we consider two network motifs and weight them accordingly with the derived w_{ij} and w_{ijk}. In order to compute these, we evaluate angles between the involved segments – denoted with $\boldsymbol{\gamma}_{ij}$ and $\boldsymbol{\gamma}_{ijk}$ (cf. Fig. 3c) – under consideration of their estimated radii and define:

$$w_{ij} = -\log\frac{p_{C,ij}}{p_T} = -\log\frac{P\left(\boldsymbol{\gamma}_{ij}|\text{continue},\Theta\right)P(\text{continue}|\Theta)}{P\left(\boldsymbol{\gamma}_{ij}|\text{terminate},\Theta\right)P(\text{terminate}|\Theta)}, \quad (18)$$

$$w_{ijk} = -\log\frac{p_{B,ijk}p_T^2}{p_{C,ij}p_{C,ik}p_{C,jk}} \quad (19)$$

$$= -\log\frac{P\left(\boldsymbol{\gamma}_{ijk}|\text{branch},\Theta\right)P(\text{branch}|\Theta)P(\text{terminate}|\Theta)^2}{\prod_{(i',j')\in 2^{\{i,j,k\}}}P\left(\boldsymbol{\gamma}_{i'j'}|\text{continue},\Theta\right)P(\text{continue}|\Theta)}, \quad (20)$$

where Θ is the parametric model that encodes physiologically realistic geometric properties of the network motifs in terms of distributions over the considered geometric features $\boldsymbol{\gamma}_{ij}$ and $\boldsymbol{\gamma}_{ijk}$. The probabilities $p_{C,ij}$, $p_{B,ijk}$ and p_T originate from the definitions in (5) and (6). In this case, $P(\boldsymbol{\gamma}_{ij}|\text{continue},\Theta)$ describes the likelihood of observing angle $\boldsymbol{\gamma}_{ij}$ in a continuing pair, and $P(\text{continue}|\Theta)$ is the prior on how frequent continuing pairs occur. We will discuss the choice of such a model Θ in our experiments (Section 3.3) where we fit them to evidence from high-resolution network data.

2.2.4. Global connectivity

An essential aspect when extracting vascular networks from noisy or incomplete data is to enforce connectivity between the observed components in the network. In our approach, we enforce this property by hard constraints:

$$\sum_{x_i\in M}x_i < |M| + \sum_{x_j\in N}x_j \quad \forall M\subset X\setminus x_{\text{seed}}, \quad (21)$$

where M is a set of connected segments and N its neighborhood. In other words, a subset M of segments that form one connected structure can only be active, if there is an incoming segment (or it is adjacent to the seed). As there are exponentially many constraints, we follow a lazy constraint generation approach and iteratively add those which are required (cf. Section 2.2.6).
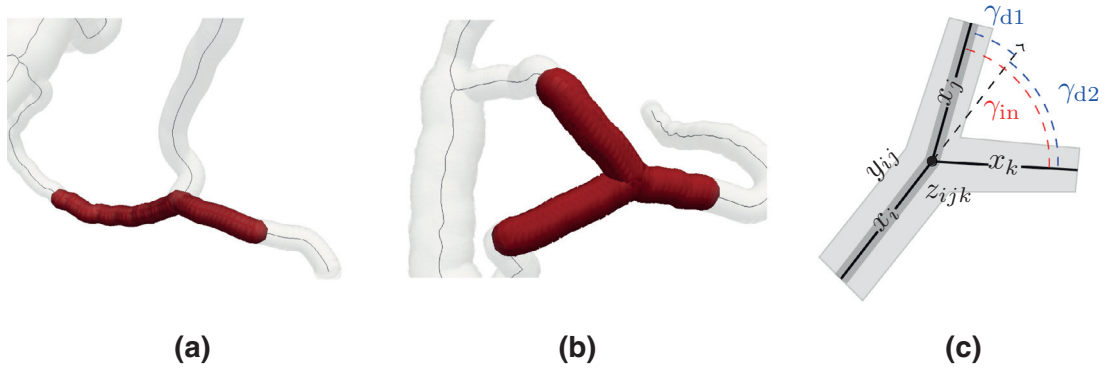
Fig. 3. Illustration of network motifs that are considered by the physiological model and the variables at a potential bifurcation. (a) Pairs of continuing segments and (b) triplets that form a bifurcation (illustrated in red). (c) Variables at a potential bifurcation: Segments, e.g. x_i, are drawn as solid black lines, while a pairwise variable y_{ij} that represents x_i continuing in x_j is depicted by the dark grey overlay (y_{ik} and y_{jk} are omitted for clarity). z_{ijk} corresponds to all three adjacent edges in the bifurcation (light grey). Furthermore, both deviation angles γ_d (blue) and the inner angle γ_{in} (red) are shown. Radii are estimated perpendicular to the edge direction. In our experiments, we consider geometric features $\boldsymbol{\gamma}_{ijk} = (\gamma_{in}, \gamma_{d1}, \gamma_{d2})_{ijk}$ for bifurcations and $\boldsymbol{y}_{ij} = (\gamma_d)_{ij}$ for continuing segments, while radius estimates are used to determine the main trunk. (Best viewed in color in the web version of this article.)

2.2.5. Linear formulation

We note that the integer program in (11) contains second and third order relations between variables. To deal with these, we exploit the binary nature of the variables x_i and introduce additional auxiliary variables $Y = \{y_{ij}\}$ and $Z = \{z_{ijk}\}$ to substitute these products ($x_i x_j$ and $x_i x_j x_k$) in the objective. A set of linear constraints ties the auxiliary variables to the corresponding indicator variables $\{x_i\}$ such that $y_{ij} = x_i x_j$ and $z_{ijk} = x_i x_j x_k$ holds for all feasible solutions:

$$y_{ij} \leq x \quad \forall x \in \{x_i, x_j\}, \forall y_{ij} \in Y, \tag{22}$$

$$y_{ij} \geq x_i + x_j - 1 \quad \forall y_{ij} \in Y, \tag{23}$$

$$z_{ijk} \leq x \quad \forall x \in \{x_i, x_j, x_k\}, \forall z_{ijk} \in Z, \tag{24}$$

$$z_{ijk} \geq x_i + x_j + x_k - 2 \quad \forall z_{ijk} \in Z, \tag{25}$$

which leads to the ILP:

$$J(\mathbf{x}, \mathbf{y}, \mathbf{z}) = \alpha \sum_{x_i \in X} w_i x_i + \sum_{y_{ij} \in Y} w_{ij} y_{ij} + \sum_{z_{ijk} \in Z} w_{ijk} z_{ijk}, \tag{26}$$

$$\text{s.t.} \quad \mathbf{A}'(\mathbf{x}, \mathbf{y}, \mathbf{z}) \geq \mathbf{b}', \tag{27}$$

$$x_i \in \{0, 1\} \quad \forall x_i \in X, \tag{28}$$

$$y_{ij} \in \{0, 1\} \quad \forall y_{ij} \in Y, \tag{29}$$

$$z_{ijk} \in \{0, 1\} \quad \forall z_{ijk} \in Z, \tag{30}$$

where we summarized the constraints (22)–(25) together with (12) in (27). $(\mathbf{x}, \mathbf{y}, \mathbf{z})$ is the concatenation of all binary variables to a column vector of all variables. We can solve the linear problem of (26) by a branch and cut algorithm implemented in libraries such as IBM ILOG CPLEX Optimizer (2014).

2.2.6. Solving the integer programming problem for large datasets

The described integer programming problem of (26) with the associated constraints grows quickly for large graphs that result from whole brain scans. To tackle this problem, we propose to employ a lazy constraint generation scheme together with the following approach:

1. Given the variable set X of the ILP, define a graph $A = (V_A, E_A)$ with a vertex $v_i \in V_A$ for every $x_i \in X$.
2. Add an edge e_{ij} to E_A if and only if there exists a constraint that contains both variables x_i and x_j.
3. Determine the connected components in A. Vertices of each connected component represent a sub-problem that can be solved independently – of course with their according constraints.

Whenever a constraint or variable is added, we adjust the graph A dynamically. Then only sub-problems – i.e. variable sets represented by connected components of A that are affected by the change – need to be solved, speeding up the performance over approaches that solve the complete problem in every run. Lazy constraint generation is a known concept in integer programming, which was, for example, already applied to the famous travelling salesman problem (Miliotis, 1976), whereas the dynamic sub-problem handling is novelty of our approach. Employing this scheme does not deteriorate the solutions quality, that is its objective value in terms of the cost function $J(.)$ in (11). However, the solution $\mathbf{x}^*$ is in general not unique and hence, solutions obtained from different optimizers are not necessarily identical in terms of the network that they encode.

3. Experiments

3.1. Image data

We use four 3-D in-vivo μMRA images of the mouse brain, each of size 248 px $\times$ 248 px $\times$ 109 px with an isotropic voxel spacing of 60 μm, and a micro computed tomography (μCT) of a corrosion cast from the cerebral vasculature of a mouse brain with a volume of 2048 px $\times$ 2048 px $\times$ 3714 px and a spacing of 2.9 μm. Both image data types are depicted in Fig. 4. All five datasets were acquired from different animals with one acquisition protocol for all μMRA images. The μCT is downsampled by a factor of 2 for the subsequent steps.

3.2. Preprocessing: vessel segmentation and graph construction

We use the described vessel segmentation framework (Schneider et al., 2013, 2015) to obtain an initial segmentation and to construct network graphs. Its parameters, such as SFT order and scales as well as RF parameters, are adjusted in a leave-one-out cross-validation using manually annotated ground truth labels. Probability maps $P(I)$ are binarized for different thresholds θ and transformed into network graphs using DOHT as discussed in Section 2.1. We segment and track vessels in both μMRA and the μCT volume. The non-overconnected results, obtained from single thresholds $\{0.2, 0.5, 0.9\}$, – denoted as *alternative* below – serve as comparison in the experiments.

3.3. Training: learning the geometric prior from the high resolution network

We use the geometrical prior to support bifurcations in our overconnected graph that are valid with respect to their diameter and relative angle, and to remove those that are not. To this end, we learn the
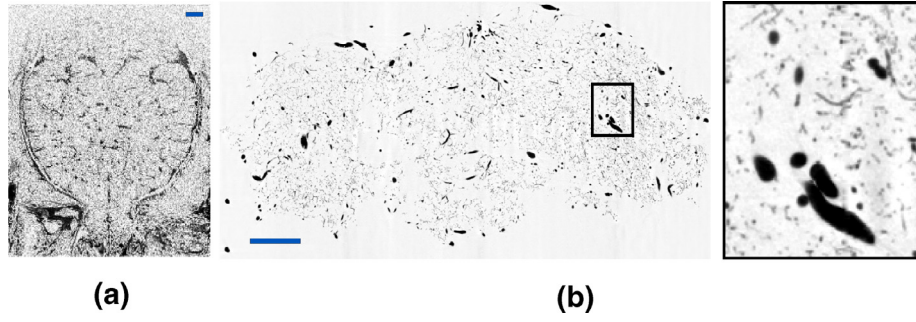
Fig. 4. (a) Example slice of a whole-brain μMRA dataset, (b) central slice of the corrosion cast μCT with a magnified subregion (right). All images are gray-scale inverted and the scalebar is 1 mm.
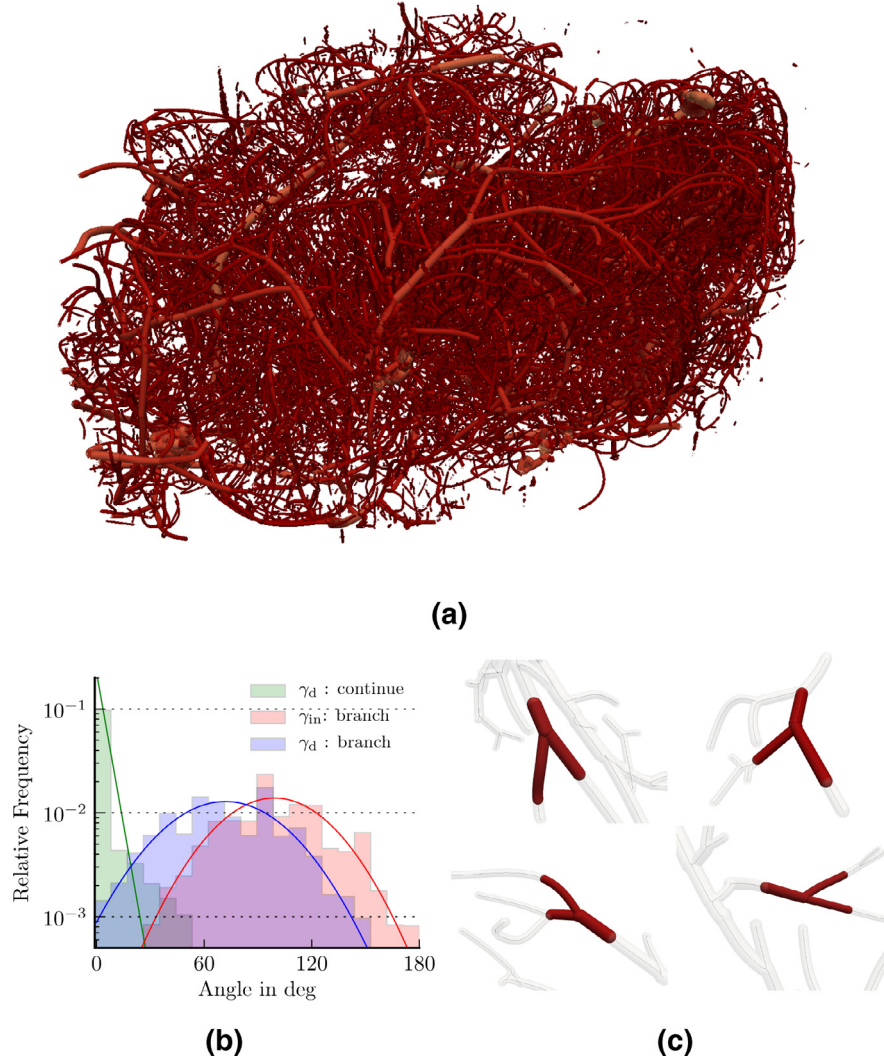

Fig. 5. (a) Processed network of the corrosion cast μCT; see Fig. 4 for scale. (b) Angle histograms computed on the extracted network of the corrosion cast dataset with inferred distributions (solid). Shown are deviation angles of continuing segments (green), deviation (blue) and inner (red) bifurcation angles (see Fig. 3c). (c) Favorable configurations of bifurcations (red) according to the fitted model of the corrosion cast μCT. (Best viewed in color in the web version of this article.)

relative frequencies of radii and deviation angles of vessel segments from the high resolution μCT (see Fig. 5b for observed angles). We find $p(\gamma_{ij}|\text{continue}, \Theta)$ to be well represented by an exponential distribution (where γ_{ij} is the deviation angle between two continuing vessels), and $p(\boldsymbol{\gamma}_{ijk}|\text{branch}, \Theta)$ to be well approximated by a multivariate Gaussian (where $\boldsymbol{\gamma}_{ijk}$ are the three angles of a bifurcation) while Θ is the joint set of parameters of the two distribution models. Radius estimates are utilized to determine the main trunk in a bifurcation

that serves as the reference for the angles considered here. An illustration of the angles calculated at every possible bifurcation is given in Fig. 3c. Furthermore, we estimate the relative frequencies of the discussed network motifs, $P(\text{continue}|\Theta)$, $P(\text{branch}|\Theta)$ and $P(\text{terminate}|\Theta)$. For this, we take into account that paths in the high-resolution data (n-times higher spatial resolution) are more frequently sampled due to the higher spatial resolution, while the number of bifurcation points remains constant. Hence, for estimating
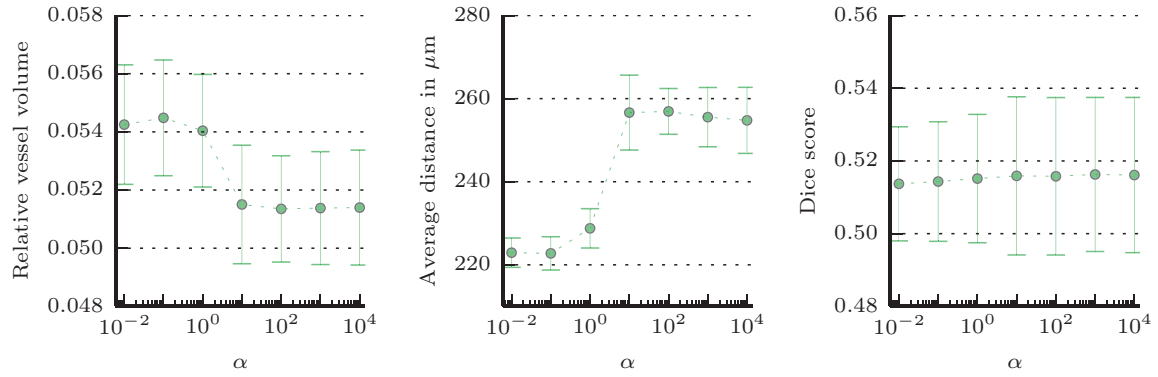
Fig. 6. Sensitivity study on the weight parameter α performed on two μMRA datasets. The parameter α has a limited impact with respect to the depicted scores. Averages are within 5.13% and 5.45% for relative vessel volume, 222 μm and 256 μm average distance and 51.4% and 51.6% Dice (cf. Fig. 8).
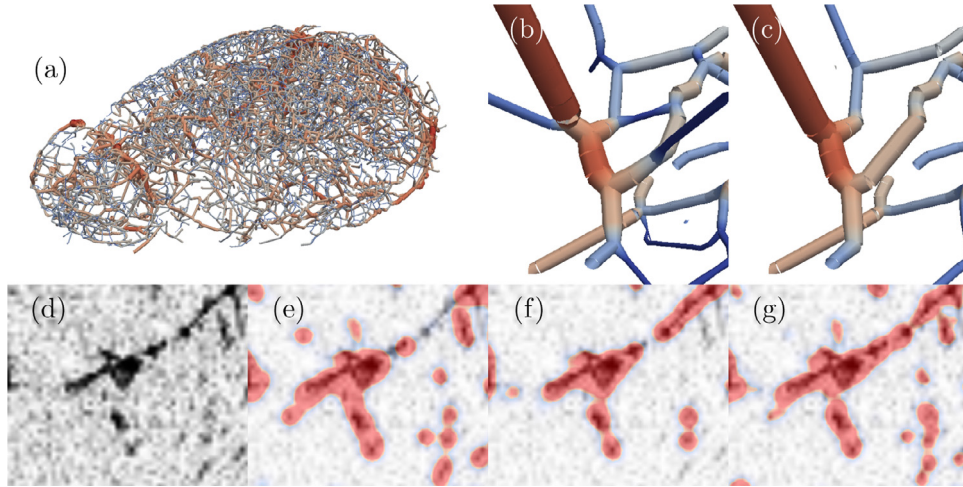

Fig. 7. Visualization of the results. (a) Rendered vascular network extracted with our method (opt, $\alpha = 1$). (b) Detail view before and (c) after optimization. Colors change with vessel diameter. (d) Raw image. (e) Rasterized DOHT network $\theta = 0.5$ and (f) with $\theta = 0.9$. (g) Postprocessed network with our method. Note that for the rasterization, a simple tube model is used and therefore, not a perfect voxel-grained segmentation is to be expected but rather a qualitative visualization that indicates whether or not a structure is present in the network model (shown as red overlay). (Best viewed in color in the web version of this article.)

$P(\text{continue}|\Theta)$, we normalize the number of points sampled along paths by the resolution ratio n between high and low resolution datasets. Otherwise, $P(\text{continue}|\Theta)$ would be strongly overestimated for the low-resolution data. Parameters Θ are fitted to the distributions observed in the μCT using the maximum likelihood estimate. The fitted model is then used to determine weights w_{ij} and w_{ijk} as in (18) and (20). Samples of favorable network motifs according to the learned distributions are depicted in red in Fig. 5c.

3.4. Application: extracting networks from low resolution μMRA data

We generate an overconnected graph for each of the μMRA test sets using the approach described in Section 2.1 with multiple thresholds $\theta_i \in \{0.2, 0.5, 0.9\}$. We select these three thresholds to obtain connections from high-recall ($\theta = 0.2$), high-precision ($\theta = 0.9$) and trade-off ($\theta = 0.5$) binarizations. After optimization (with $\alpha = 1$ and a maximal $\alpha_{max} = \alpha \to \infty$), we compare the extracted network (opt) to networks obtained from individual thresholds $\theta = 0.2, 0.5$ and 0.9 (alternative).

We present a sensitivity analysis of the α-parameter of our method in Fig. 6. For large values of α, the image evidence is emphasized (the network is still connected), while choosing a small value of α prioritizes geometric weights. Although varying α has limited impact on the scores that we calculate for our test data, it is recommendable for other problems to determine the most suitable α depending on the previously applied processing, namely the segmentation and over-

connection stage. If the data to be processed is expected to contain malformations that are known to form atypical bifurcations, then it would not be advisable to choose $\alpha < 1$, unless the prior model had been adapted accordingly. In the following experiments, we will set $\alpha = 1$ per default and compute results with α_{max} – i.e. maximum emphasis on the image evidence term – for comparison.

Fig. 7a shows an optimized network, while Fig. 7b and c provides close-up views before and after optimization, respectively. A number of spurious sprouts and loops are visible that are removed during the process. Details in Fig. 7d–g show differences between the two thresholded and an optimized network. We find that both thresholded networks (Fig. 7e and f) lose the connection of the large branch (center to top-right), while it is retained in the optimized network (Fig. 7g).

Fig. 8 reports quantitative measures of global network properties, such as relative vessel volume, average distance to the next vessel (i.e. extravascular distance) and Dice score. We calculate both relative vessel volume and the extravascular distance over a manually annotated brain mask of 360 mm^3. In order to compute Dice scores, we rasterize the networks using a tubular model of circular shape and compare them with voxel-grained annotations that were obtained manually on a set of selected slices along each direction. As a consequence of this rasterization, inaccuracies on the voxel level are introduced that negatively affect absolute values of the Dice score, which is already very sensitive for thin structures such as vessels. Note, however, that all compared strategies are affected by this to the same degree. We find the optimized network (opt, $\alpha = 1$) to always
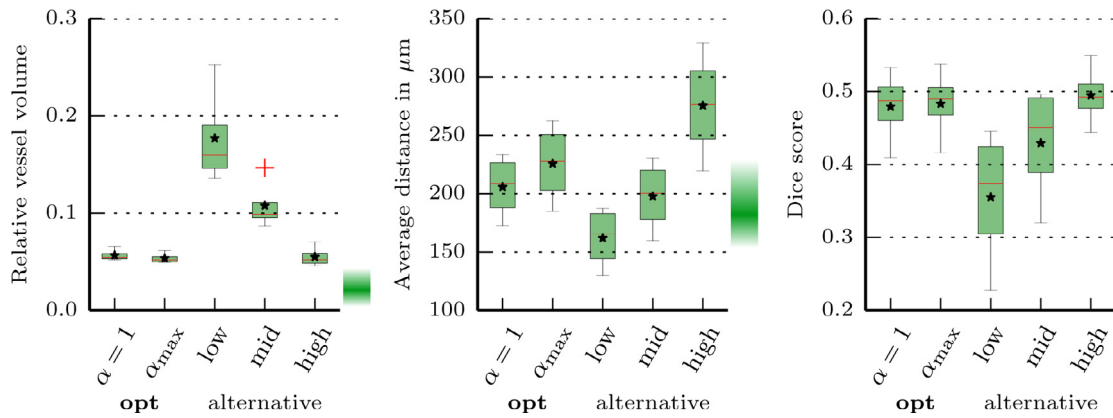
Fig. 8. Comparison between the optimized networks (opt) with $\alpha = 1$, $\alpha_{max} = \alpha \to \infty$ and simple networks obtained at thresholds $\theta = 0.2$, 0.5 and 0.9 (alternative: low = 0.2, mid = 0.5, high = 0.9). Boxplots (median as red line, mean as $\star$) depict the statistics on all four μMRA datasets. The gradients (green) to the right of both plots of physiological scores indicate physiologically plausible ranges (cf. Heinzer et al. (2006)). The Dice score has been computed by comparing voxel-wise annotations with the rasterized the networks using a simple tube model (negatively affecting absolute Dice values for all approaches to the same degree). Our regularization (opt, $\alpha = 1$) always groups with the more favorable of the alternatives, i.e. it has a small vessel volume, a moderate average distance and yet an acceptable high Dice score.

Table 1

Runtimes in minutes on different μMRA datesets for our proposed solving scheme (t_{ilpcc}) and an off-the-shelf solver (t_{cplex}). We observe that our method is faster as the off-the-shelf solver in the majority of cases.

Dataset	# 1	# 2	# 3	# 4
t_{ilpcc}	2060.6	186.0	18.6	8.8
t_{cplex}	2958.6	385.0	31.6	8.7
$\frac{t_{cplex}-t_{ilpcc}}{t_{ilpcc}}$	0.44	1.07	0.70	− 0.01

group with the more favorable of the alternative, which is a low vessel volume, a moderate, i.e. neither too small nor too large, extravascular distance and a high Dice score, while each of the alternative approaches provides poor results in at least one of these scores. The relative vessel volumes vary between 5.2% and 6.5% for our datasets, while Heinzer et al. (2006) reported values from 3.6% to 4.2% and also observed some inter-subject variability. Comparing the result of our optimization with parameter $\alpha = 1$ and the maximal choice of α_{max}, we observe that both relative vessel volume and Dice score vary only slightly, while the average distance increases when using α_{max}, hence resulting in networks with a decreased vascular density. While the results support the assumption that combining image evidence with geometric prior benefits network extraction, it will require analysis on more extensive databases to quantify the methods robustness in presence of specific pathologies and malformations.

Comparing the processing time of the proposed solver (Section 2.2.6) and a standard method (IBM ILOG CPLEX V12.51 (IBM ILOG CPLEX Optimizer, 2014)) as reported in Table 1, we find that our approach of handling subproblems during the optimization leads to an improvement: runtimes (one run each, on a quadcore CPU, 32 GB RAM) were shorter in three out of four cases, whereas the standard method took between 44% and 107% longer. We find that absolute run times may vary widely depending on the size of the overconnected graph and its connectedness as well as parametrization due to the dynamic processing scheme. For those two datasets that run much longer (# 1 and # 2), we observe that the number of removed segments is two to three times higher than for the two others, while the resulting, optimized networks describe all a very similar vascular volume (as seen in Fig. 8). We attribute this to a situation where the overconnection scheme is not as efficient as for the two latter datasets and a high number of connections has to be discarded in the regularization. The relative runtimes indicate that the approach of partitioning the ILP into independent subproblems

yields larger gains on datasets which required more iterations in the constraint generation, i.e. had longer absolute runtimes.

4. Conclusions[1]

We have introduced a probabilistic approach for extracting vessel networks and we can compute the MAP estimate efficiently by solving an ILP. We learned physiological-geometric properties considered in the probabilistic model from a high-resolution corrosion cast μCT of a murine cerebrovascular network and applied it to low-resolution, in-vivo μMRA images, leading to superior extracted networks in terms of macroscopic measures.

Our method can be applied as post-processing step to existing vessel segmentation pipelines in order to incorporate physiological knowledge for improved network extraction. As such, it can be combined with other graph generation methods that are potentially able to overconnect the graph, such as discussed in Kaufhold et al. (2012) and Schneider et al. (2014). It can be used with any other geometrical–physiological prior knowledge about properties, for example considering vessel shape, length, curvature and flow direction, or a non-parametric learning as in Lu et al. (2009). Even a spatially-variant prior could be designed and incorporated to address different vascular properties in certain areas, similar to the parametric maps used for latent classes in Menze et al. (2010) and Riklin-Raviv et al. (2010). Furthermore, higher-order network motifs that occur frequently in vasculature could be included into the prior model in the same way as bifurcations. It should be noted, however, that increasing the complexity of the prior model would likely require a larger database for training.

For future studies, it would be interesting to assess the robustness of the approach with respect to specific pathologies and abnormalities in the vascular network. Another direction could be the extension of the algorithm to jointly infer a subject-specific parametrization of the physiological model and predict the underlying network.

---

[1] A version of our network optimization code will become available from: http://ibbm.in.tum.de/software.

Appendix A

In Section 2.2.2, we found that the MAP estimate $\mathbf{x}^*$ is given by

$$\mathbf{x}^* = \arg\max_{\mathbf{x}\in\Omega} P(\mathbf{X} = \mathbf{x}|I, G). \tag{31}$$

Here, we are going to derive the cost function from the definition of the MRF (3). We start by using the definitions of the potential functions $\phi(\,\cdot\,)$, (4)–(6), in the logarithm of $P(\mathbf{X} = \mathbf{x}|I, G)$:

$$
\begin{aligned}
\log P\left(\mathbf{X} = \mathbf{x}|I, G\right) \propto \\
\alpha \sum_{x_i \in X} \log\left(P\left(x_i = 1|I_i, E_i\right)^{x_i} P\left(x_i = 0|I_i, E_i\right)^{1-x_i}\right) \\
+ \sum_{\substack{x_i,x_j\in X:\\ e_i,e_j \text{ adjacent}\\ \nexists e_k \text{ adjacent to } e_i\wedge e_j}} \log\left(p_{C,ij}^{x_ix_j} p_T^{1-x_ix_j}\right) \\
+ \sum_{\substack{x_i,x_j,x_k\in X:\\ e_i,e_j,e_k \text{ adjacent}}} \log\left(p_{B,ijk}^{x_ix_jx_k} p_T^{(1-x_i)(1-x_j)(1-x_k)} \prod_{(i',j')\in S} p_{C,i'j'}^{x_{i'}x_{j'}-x_ix_jx_k}\right)
\end{aligned} \tag{32}
$$

$$
\begin{aligned}
= \alpha \sum_{x_i\in X} x_i \log \frac{P\left(x_i = 1|I_i, E_i\right)}{P\left(x_i = 0|I_i, E_i\right)} + \log P\left(x_i = 0|I\right) \\
+ \sum_{\substack{x_i,x_j\in X:\\ e_i,e_j \text{ adjacent}\\ \nexists e_k \text{ adjacent to } e_i\wedge e_j}} x_ix_j \log \frac{p_{C,ij}}{p_T} + \log p_T \\
+ \sum_{\substack{x_i,x_j,x_k\in X:\\ e_i,e_j,e_k \text{ adjacent}}} \left(x_ix_jx_k \log \frac{p_{B,ijk}p_T^2}{\prod_{(i',j')\in S} p_{C,i'j'}}\right. \\
\left. + \sum_{(i',j')\in S} \left(x_{i'}x_{j'} \log \frac{p_{C,i'j'}}{p_T}\right) + \log p_T\right),
\end{aligned} \tag{33}
$$

where we applied multilinear representations for pseudo-boolean functions and S is the set of pairs out of $\{i, j, k\}$, i.e. $S = 2^{\{i, j, k\}}$. Discarding the constant terms, rearranging the pairwise terms originating from the ternary potentials and merging them with the uniquely pairwise terms – which generates per definition no doubles – then leads to

$$
\begin{aligned}
\log P\left(\mathbf{X} = \mathbf{x}|I, G\right) \propto \\
\alpha \sum_{x_i\in X} x_i \log \frac{P\left(x_i = 1|I_i, E_i\right)}{P\left(x_i = 0|I_i, E_i\right)} + \sum_{\substack{x_i,x_j\in X:\\ e_i,e_j \text{ adjacent}}} x_ix_j \log \frac{p_{C,ij}}{p_T}
\end{aligned} \tag{34}
$$

$$
+ \sum_{\substack{x_i,x_j,x_k\in X:\\ e_i,e_j,e_k \text{ adjacent}}} x_ix_jx_k \log \frac{p_{B,ijk}p_T^2}{p_{C,ij}p_{C,ik}p_{C,jk}}. \tag{35}
$$

Finally, taking the negative logarithm turns the maximization into a minimization:

$$\mathbf{x}^* = \arg\min_{\mathbf{x}\in\Omega} -\log P(\mathbf{X} = \mathbf{x}|I, G) \tag{36}$$

$$
= \arg\min_{\mathbf{x}\in\Omega} \alpha \sum_{x_i\in X} -\log \frac{P\left(x_i=1|I_i,E_i\right)}{P\left(x_i=0|I_i,E_i\right)} x_i + \sum_{\substack{x_i,x_j\in X:\\ e_i,e_j \text{ adjacent}}} -\log \frac{p_{C,ij}}{p_T} x_ix_j \tag{37}
$$

$$
+ \sum_{\substack{x_i,x_j,x_k\in X:\\ e_i,e_j,e_k \text{ adjacent}}} -\log \frac{p_{B,ijk}p_T^2}{p_{C,ij}p_{C,ik}p_{C,jk}} x_ix_jx_k, \tag{38}
$$

which is equivalent to the integer program:

$$
\begin{aligned}
\min_{\mathbf{x}} \quad J(\mathbf{x}) = \alpha \sum_{x_i\in X} w_i x_i + \sum_{\substack{x_i,x_j\in X:\\ e_i,e_j \text{ adjacent}}} w_{ij}x_ix_j \\
+ \sum_{\substack{x_i,x_j,x_k\in X:\\ e_i,e_j,e_k \text{ adjacent}}} w_{ijk}x_ix_jx_k,
\end{aligned} \tag{39}
$$

$$\text{s.t.} \quad \mathbf{Ax} \geq \mathbf{b}, \tag{40}$$

$$x_i \in \{0, 1\} \qquad \forall x_i \in X, \tag{41}$$

with the weights given as:

$$w_i = -\log \frac{P\left(x_i=1|I_i,E_i\right)}{P\left(x_i=0|I_i,E_i\right)}, \tag{42}$$

$$w_{ij} = -\log \frac{p_{C,ij}}{p_T}, \tag{43}$$

$$w_{ijk} = -\log \frac{p_{B,ijk}p_T^2}{p_{C,ij}p_{C,ik}p_{C,jk}}. \tag{44}$$

Supplementary materials

Supplementary material associated with this article can be found, in the online version, at 10.1016/j.media.2015.03.008.

References

Alon, U., 2007. Network motifs: theory and experimental approaches. Nat. Rev. Genet. 8 (6), 450–461.

Aylward, S.R., Bullitt, E., 2002. Initialization, noise, singularities, and scale in height ridge traversal for tubular object centerline extraction. IEEE Trans. Med. Imag. 21, 61–75.

Benmansour, F., Cohen, L.D., 2011. Tubular structure segmentation based on minimal path method and anisotropic enhancement. Int. J. Comput. Vis. 92 (2), 192–210.

Cohen, L.D., Kimmel, R., 1997. Global minimum for active contour models: a minimal path approach. Int. J. Comput. Vis. 24 (1), 57–78.

Frangi, A., Niessen, W., Vincken, K., Viergever, M., 1998. Multiscale vessel enhancement filtering. In: Wells, W., Colchester, A., Delp, S. (Eds.), Medical Image Computing and Computer-Assisted Intervention MICCAI 1998, LNCS 1496. Springer, Berlin/Heidelberg, pp. 130–137.

Gülsün, M.A., Tek, H., 2008. Robust vessel tree modeling. In: Medical Image Computing and Computer-Assisted Intervention–MICCAI 2008, LNCS 5241. Springer, pp. 602–611.

Heinzer, S., Krucker, T., Stampanoni, M., Abela, R., Meyer, E.P., Schuler, A., Schneider, P., Müller, R., 2006. Hierarchical microimaging for multiscale analysis of large vascular networks. Neuroimage 32.2, 626–636.

Hunter, J.M., Kwan, J., Malek-Ahmadi, M., Maarouf, C.L., Kokjohn, T.A., Belden, C., Sabbagh, M.N., Beach, T.G., Roher, A.E., 2012. Morphological and pathological evolution of the brain microcirculation in aging and Alzheimer's disease. PLoS ONE 7, E36893.

IBM ILOG CPLEX Optimizer. http://www.ibm.com/software/integration/optimization/cplex-optimizer/, 2014.

Jiang, Y., Zhuang, Z., Sinusas, A., Papademetris, X., 2010. Vascular tree reconstruction by minimizing a physiological functional cost. In: Computer Vision and Pattern Recognition Workshops (CVPRW).

Jiang, Y., Zhuang, Z.W., Sinusas, A.J., Staib, L.H., Papademetris, X., 2011. Vessel connectivity using Murray's hypothesis. In: Medical image computing and computer-assisted intervention – MICCAI 2011. LNCS 6893. Springer, Berlin/Heidelberg, pp. 528–536.

Kaufhold, J.P., Tsai, P.S., Blinder, P., Kleinfeld, D., 2012. Vectorization of optically sectioned brain microvasculature: learning aids completion of vascular graphs by connecting gaps and deleting open-ended segments. Med. Image Anal. 16 (6), 1241–1258.

Kirbas, C., Quek, F., 2004. A review of vessel extraction techniques and algorithms. ACM Comput. Surveys (CSUR) 36 (2), 81–121.

Klohs, J., Baltes, C., Princz-Kranz, F., Ratering, D., Nitsch, R.M., Knuesel, I., Rudin, M., 2012. Contrast-enhanced magnetic resonance microangiography reveals remodeling of the cerebral microvasculature in transgenic arcaβ mice. J. Neurosci. 32 (5), 1705–1713.

Lee, T., Kashyap, R., Chu, C., 1994. Building skeleton models via 3-d medial surface axis thinning algorithms. CVGIP: Graph. Models Image Process. 56.6, 462–478.

Lesage, D., Angelini, E., Bloch, I., Funka-Lea, G., 2009. A review of 3d vessel lumen segmentation techniques: models, features and extraction schemes. Med. Image Anal. 13 (6), 819–845.

Lu, L., Bi, J., Yu, S., Peng, Z., Krishnan, A., Zhou, X.S., 2009. Hierarchical learning for tubular structure parsing in medical imaging: a study on coronary arteries using 3d ct angiography. In: 2009 IEEE 12th International Conference on Computer Vision, pp. 2021–2028.

Menze, B., Kelm, B., Splitthoff, D., Koethe, U., Hamprecht, F., 2011. On oblique random forests. In: Gunopulos, D., Hofmann, T., Malerba, D., Vazirgiannis, M. (Eds.), Machine Learning and Knowledge Discovery in Databases, LNCS 6912. Springer, Berlin/Heidelberg, pp. 453–469.

Menze, B.H., Leemput, K.V., Lashkari, D., Weber, M.A., Ayache, N., Golland, P., 2010. A generative model for brain tumor segmentation in multi-modal images. In: Medical image computing and computer-assisted intervention – MICCAI 2010. LNCS 6801. Springer, Berlin/Heidelberg, pp. 151–159.

Miliotis, P., 1976. Integer programming approaches to the travelling salesman problem. Math. Program. 10 (1), 367–378.

Milo, R., Shen-Orr, S., Itzkovitz, S., Kashtan, N., Chklovskii, D., Alon, U., 2002. Network motifs: simple building blocks of complex networks. Science (New York, N.Y.) 298 (5594), 824–827.

Murray, C.D., 1926. The physiological principle of minimum work: I. The vascular system and the cost of blood volume. Proc. Natl. Acad. Sci. USA 12 (3), 207.

Pudney, C., 1998. Distance-ordered homotopic thinning: a skeletonization algorithm for 3d digital images. Comput. Vis. Image Und. 72 (3), 404–413.

Qu, L., Andres, B., 2014. Estimating maximally probable constrained relations by mathematical programming, (2014). http://arxiv.org/abs/1408.0838.

Riklin-Raviv, T., Leemput, K.V., Menze, B.H., Wells, W.M., Golland, P., 2010. Segmentation of image ensembles via latent atlases. Med. Image Anal. 14 (5), 654–665.

Schneider, M., Hirsch, S., Székely, G., Weber, B., Menze, B.H., 2013. Oblique random forests for 3-D vessel detection using steerable filters and orthogonal subspace filtering. In: Menze, B.H., Langs, G., Montillo, A., Tu, Z., Criminisi, A. (Eds.), MICCAI 2012 – Workshop on Medical Computer Vision. Springer, Heidelberg/Berlin, pp. 142–154.

Schneider, M., Hirsch, S., Weber, B., Székely, G., Menze, B.H., 2015. Joint 3-D vessel segmentation and centerline extraction using oblique Hough forests with steerable filters. Med. Image Anal. 19 (1), 220–249.

Schneider, M., Hirsch, S., Weber, B., Székely, G., Menze, B.H., 2014. TGIF: topological gap in-fill for vascular networks – a generative physiological modeling approach. In: Medical Image Computing and Computer-Assisted Intervention – MICCAI. LNCS 8674. Springer, Berlin/Heidelberg, pp. 89–96.

Stühmer, J., Schröder, P., Cremers, D., 2013. Tree shape priors with connectivity constraints using convex relaxation on general graphs. In: International Conference on Computer Vision (ICCV), pp. 2336–2343.

Türetken, E., Benmansour, F., Andres, B., Pfister, H., Fua, P., 2013. Reconstructing loopy curvilinear structures using integer programming. In: 2013 IEEE Conference on Computer Vision and Pattern Recognition (CVPR), IEEE, pp. 1822–1829.